

Highly mobile ferroelastic domain walls in compositionally graded ferroelectric thin films

J. C. Agar^{1,2}, A. R. Damodaran¹, M. B. Okatan³, J. Kacher^{1,4}, C. Gammer^{1,4}, R. K. Vasudevan³, S. Pandya¹, L. R. Dedon¹, R. V. K. Mangalam¹, G. A. Velarde², S. Jesse³, N. Balke³, A. M. Minor^{1,4}, S. V. Kalinin³ and L. W. Martin^{1,5*}

Domains and domain walls are critical in determining the response of ferroelectrics, and the ability to controllably create, annihilate, or move domains is essential to enable a range of next-generation devices. Whereas electric-field control has been demonstrated for ferroelectric 180° domain walls, similar control of ferroelastic domains has not been achieved. Here, using controlled composition and strain gradients, we demonstrate deterministic control of ferroelastic domains that are rendered highly mobile in a controlled and reversible manner. Through a combination of thin-film growth, transmission-electron-microscopy-based nanobeam diffraction and nanoscale band-excitation switching spectroscopy, we show that strain gradients in compositionally graded $\text{PbZr}_{1-x}\text{Ti}_x\text{O}_3$ heterostructures stabilize needle-like ferroelastic domains that terminate inside the film. These needle-like domains are highly labile in the out-of-plane direction under applied electric fields, producing a locally enhanced piezoresponse. This work demonstrates the efficacy of novel modes of epitaxy in providing new modalities of domain engineering and potential for as-yet-unrealized nanoscale functional devices.

Domains and domain walls are known to greatly impact the properties of ferroic materials. In ferroelectric thin films, domains tend to form highly ordered ferroelastic domain structures that balance elastic and electrostatic energies^{1–5}. In practice, a diverse range of ferroelastic domain structures can be produced, of which the most common are 90° (in tetragonal systems)^{6–8} and 71° or 109° (in rhombohedral systems) domain walls^{9,10}. The ability to controllably produce such domain structures has been exploited to understand contributions to and how to enhance the dielectric¹¹, piezoelectric¹² and pyroelectric^{6,13} response of materials. Whereas domain walls in ferroelectrics can be considered analogous to magnetic domain walls (10–100 nm in width), ferroelectric domain walls are much smaller (1–10 nm in width), providing promise for high-density nanoscale devices derived from the unique properties of these features^{14–22}.

Utilizing ferroelastic domain walls for nanoscale devices requires that they be easily indexable (that is, spatially localized) and manipulated (that is, writable/erasable, change shape/orientation, and so on) by application of external stimuli in a controllable and repeatable manner. Whereas it has been shown that ferroelectric, 180° domain walls can be created and moved long distances²³, ferroelastic domain walls are typically elastically pinned, rendering them essentially immobile^{24–26}. Although recent work has shown it is possible to create, annihilate, and/or manipulate ferroelastic domains by local switching, these approaches have limited specificity for how or where the domain walls move^{7,27,28}. Furthermore, such domains can be defined only in a discrete number of shapes, structures and forms, as defined by the chemistry and elastic and electrostatic energies, hampering the ability to harness their functional properties.

Here, through a series of structural and spectroscopic analyses, we demonstrate how compositional and strain gradients can alter the energy landscape for ferroelastic domain formation, enabling the formation of ferroelastic domains which are highly labile and spring-like in the out-of-plane direction. Scanning transmission electron microscopy (STEM)-based studies reveal that compositionally graded $\text{PbZr}_{1-x}\text{Ti}_x\text{O}_3$ heterostructures exhibit *c/a/c/a*-like domain structures, which are perturbed by the strain gradient to form needle-like *a* domains that terminate within the film. Local probes of ferroelectricity based on band-excitation switching spectroscopy (BE-SS) reveal that homogeneous heterostructures exhibit (essentially) immobile *a* domains, nearly voltage symmetric switching response, and suppressed piezoresponse at/near the *a* domains, whereas compositionally graded heterostructures exhibit highly asymmetric switching response with *a* domains that are highly labile in the out-of-plane direction. As a result of elastic constraint of the films, these domains behave in a spring-like manner, whereby they grow (to the free surface) or contract (to the substrate) under electric-field excitation, resulting in a large piezoresponse in the vicinity of the *a* domains. Ultimately, we demonstrate a composition- and strain-gradient-based route to control both the shape and mobility of ferroelastic domains, enabling the formation of labile domain structures with large, repeatable, and localized piezoresponse. Such an ability to control the domain structure and response could enable new devices, including electro-optics^{29,30}, logic²⁵, memories³¹, and other applications^{15,32}.

To demonstrate the influence of compositional and strain gradients on the domain structure and response, we focus on two heterostructure variants: 100-nm-thick, homogeneous

¹Department of Materials Science and Engineering, University of California, Berkeley, California 94720, USA. ²Department of Materials Science and Engineering, University of Illinois, Urbana-Champaign, Urbana, Illinois 61801, USA. ³Center for Nanophase Materials Sciences, Oak Ridge National Laboratory, Oak Ridge, Tennessee 37831, USA. ⁴National Center for Electron Microscopy, Molecular Foundry, Lawrence Berkeley National Laboratory, Berkeley, California 94720, USA. ⁵Materials Science Division, Lawrence Berkeley National Laboratory, Berkeley, California 94720, USA.

*e-mail: lwmartin@berkeley.edu

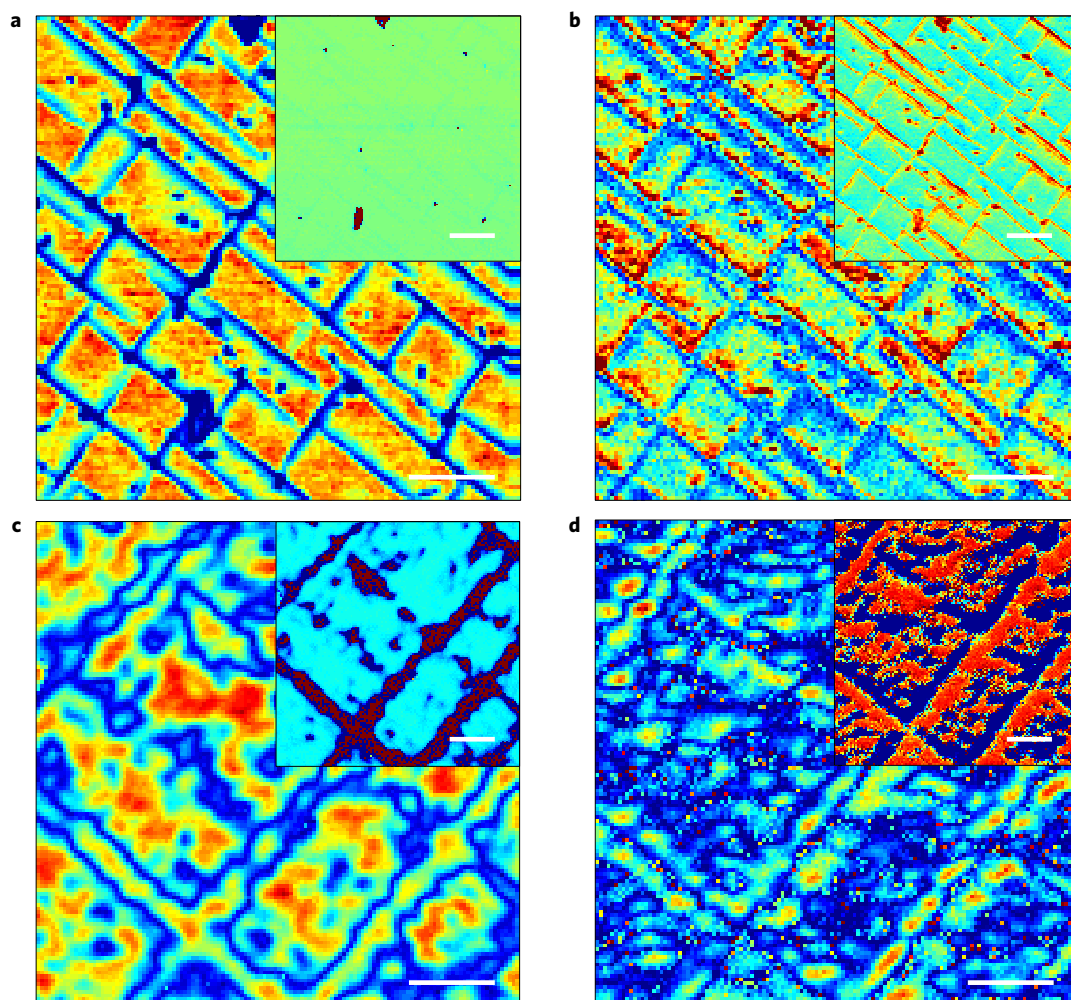


Figure 1 | Domain structures in $\text{PbZr}_{1-x}\text{Ti}_x\text{O}_3$ heterostructures. **a,b**, Band-excitation piezoresponse force microscopy images of homogeneous $\text{PbZr}_{0.2}\text{Ti}_{0.8}\text{O}_3$ heterostructures: vertical amplitude (phase inset) (**a**) and lateral amplitude (phase inset) (**b**). **c,d**, Band-excitation piezoresponse force microscopy images of compositionally graded $\text{PbZr}_{0.2}\text{Ti}_{0.8}\text{O}_3 \leftrightarrow \text{PbZr}_{0.8}\text{Ti}_{0.2}\text{O}_3$ heterostructures: vertical amplitude (phase inset) (**c**) and lateral amplitude (phase inset) (**d**). Scale bars in all images are 500 nm.

composition $\text{PbZr}_{0.2}\text{Ti}_{0.8}\text{O}_3$ heterostructures and 100-nm-thick, linear compositionally graded $\text{PbZr}_{0.8}\text{Ti}_{0.2}\text{O}_3$ (top) \leftrightarrow $\text{PbZr}_{0.2}\text{Ti}_{0.8}\text{O}_3$ (bottom) heterostructures. All heterostructures studied herein are grown on 30-nm $\text{SrRuO}_3/\text{GdScO}_3$ (110) substrates, producing an effective lattice mismatch which varies from 0.8% to -3.5% from the substrate to film surface in the compositionally graded heterostructures (see Methods and Supplementary Figs 1–4 for details; refs 9,33,34).

The ferroelectric domain structure, including both the vertical and lateral components, of the homogeneous (Fig. 1a,b) and compositionally graded (Fig. 1c,d) heterostructures were imaged using band-excitation piezoresponse force microscopy (BE-PFM, see Methods and Supplementary Fig. 5; ref. 35). Both the homogeneous and compositionally graded heterostructures reveal features reminiscent of $c/a/c/a$ domain structures which are made up of out-of-plane polarized c domains and in-plane polarized a domains separated by 90° domain walls³⁶. At first glance, the similarity of these domain structures is surprising, because at the free surface of the compositionally graded heterostructures the film is compositionally rhombohedral and should exhibit a more complex domain structure (Supplementary Fig. 6). The presence of the compositional and strain gradients can stabilize the tetragonal phase and domain structure even in a film with more than 50% of the volume compositionally on the rhombohedral side of the

phase diagram^{9,33,34}. Closer inspection reveals that the homogeneous heterostructures exhibit a highly suppressed vertical piezoresponse within the a domains as compared to the compositionally graded heterostructures, which show a similar (or enhanced) piezoresponse within the a domains. This indicates that further differences in these domain structures may be present.

Further insight into the structure of the ferroelastic domains is afforded by cross-sectional, high-angle annular dark-field (HAADF)-STEM imaging and strain mapping (see Methods). Although it has been shown^{37–39} that homogeneous $\text{PbZr}_{0.2}\text{Ti}_{0.8}\text{O}_3$ primarily forms parallelepiped-shaped ferroelastic domains with (nearly) parallel 90° domain walls along the $\{101\}$, similar studies on compositionally graded heterostructures have not been reported. HAADF-STEM images of the compositionally graded heterostructure (Fig. 2a) reveal a $c/a/c/a$ -like domain structure with exclusively wedge-like a domains that terminate within the thickness of the film (henceforth referred to as needle-like domains because of their cross-section).

Further STEM-based nanobeam diffraction studies were used to probe the local strain and strain gradients in the compositionally graded heterostructures (see Methods and Supplementary Fig. 7). Starting with the out-of-plane strain (Fig. 2b), there is evidence of a strain gradient consistent with an increasing lattice parameter from the substrate to the free surface. Similar analysis of the

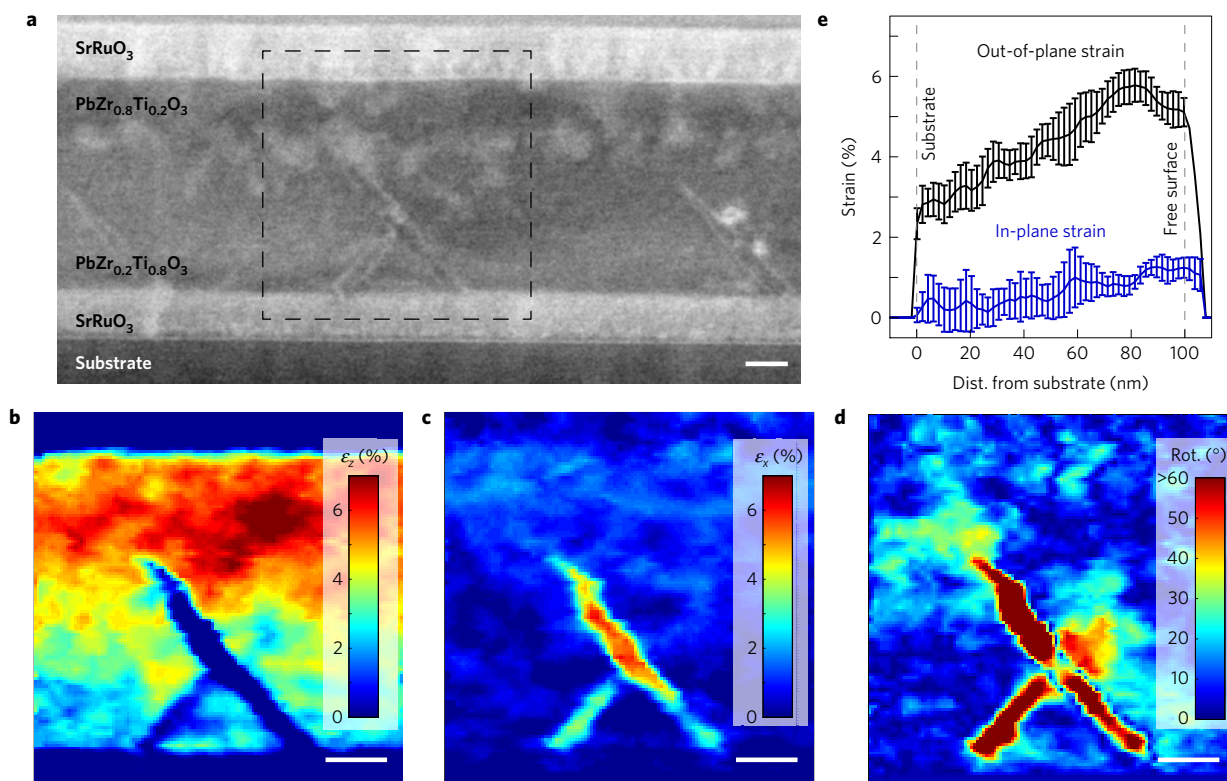


Figure 2 | Cross-sectional transmission electron microscopy studies of compositionally graded heterostructures. **a**, High-angle, angular dark-field scanning transmission electron microscopy image of a compositionally graded heterostructure revealing the presence of ferroelastic domains with needle-like shapes. **b–d**, Nanobeam diffraction-based strain mapping of compositionally graded heterostructures reveals the out-of-plane (**b**) and in-plane (**c**) strain state of the film as well as the local unit-cell rotation (**d**). All scale bars are 25 nm. **e**, Thickness-dependent, average in-plane and out-of-plane strain calculated from the nanobeam diffraction strain mapping. All strain is normalized to the substrate.

in-plane strain (Fig. 2c) reveals nearly homogeneous in-plane strain, punctuated by *a* domains which show large relative in-plane strains; however, overall the heterostructures are nearly coherently strained to the substrate. Finally, one can also map the unit-cell rotation (Fig. 2d), which shows that the *a* domains are rotated $\sim 90^\circ$ with respect to the *c* domains. Thickness-dependent averaging of the strain state (Fig. 2e) reveals out-of-plane and in-plane strain differentials of $\sim 3.8\%$ and $\sim 1.2\%$ across the film thickness, respectively. By comparing the experimentally measured in-plane lattice parameters with the bulk $\text{PbZr}_{1-x}\text{Ti}_x\text{O}_3$ lattice parameters we quantify the strain gradient to be $3.3 \times 10^5 \text{ m}^{-1}$ (Supplementary Fig. 8). Focusing on the strain near the tip of the domain, there is evidence for increased (reduced) strain along the top (bottom) edges of the ferroelastic domain, an observation consistent with phase-field models of needle-like *a* domains⁴⁰. Furthermore, at the tip of the needle-like domain, we observe unit-cell rotation near the leading edge, an indication of a local structural instability associated with a highly energetic domain wall.

The observation of needle-like domains can be understood by considering the strain and strain gradient present in the compositionally graded heterostructures. The data show that the unit-cell tetragonality increases from the substrate to the free surface, reducing the volume fraction of *a* domains necessary to accommodate the strain, and thus causing the domain walls to taper to a point. The tapering wall is geometrically required to deviate from the ostensibly uncharged {101} and, in turn, localized polarization rotations occur to accommodate this charged domain wall. Such high-energy structures are likely to be relatively unstable and should be highly responsive under electrical/mechanical stimuli^{41,42}. Collectively, these results demonstrate the potential for compositional and strain gradients to modify the elastic conditions

of ferroelastic domain formations, thereby enabling the stabilization of needle-like domains.

To explore how the variation in ferroelastic domain shape influences the material and domain wall response, we conducted BE-SS studies (Supplementary Fig. 9). This technique measures the local piezoresponse and piezoelectric hysteresis loops using a scanning probe tip. The extracted local piezoresponse at each voltage step provides spatial maps with nanoscale resolution that can be used to visualize and understand the switching process (Supplementary Fig. 10).

To demonstrate this technique, we first investigate the homogeneous heterostructures, whose switching process is better understood. For reference, we show a representative macroscopic hysteresis loop (Fig. 3a; average piezoelectric hysteresis loops are provided, Supplementary Fig. 10). It is important to note that this hysteresis loop is nearly voltage symmetric, implying that there is no preference for the up- or down-poled state. A selection of maps of the vertical amplitude and phase of the piezoresponse at various voltages throughout the switching cycle are provided (Fig. 3b–f, movies are available online, Supplementary Movie 1). Starting with the film in the up-poled state (uniform blue phase, Fig. 3b), the amplitude is larger in the *c* domains than in the *a* domains. Application of a positive bias results in rapid 180° switching to the down-poled state (change in phase from blue to red, Fig. 3c). As the voltage increases the down-poled state saturates to a state with a similar amplitude, but an opposite phase to the initial state (uniform red, Fig. 3d). On application of a negative bias (Fig. 3e,f), this process proceeds in reverse, returning to its initial up-poled state. Although there is some evidence of random domain structure reconfiguration following the BE-SS measurements, consistent with recent reports^{7,27,28}, the vast majority of the *a* domains remain fixed.

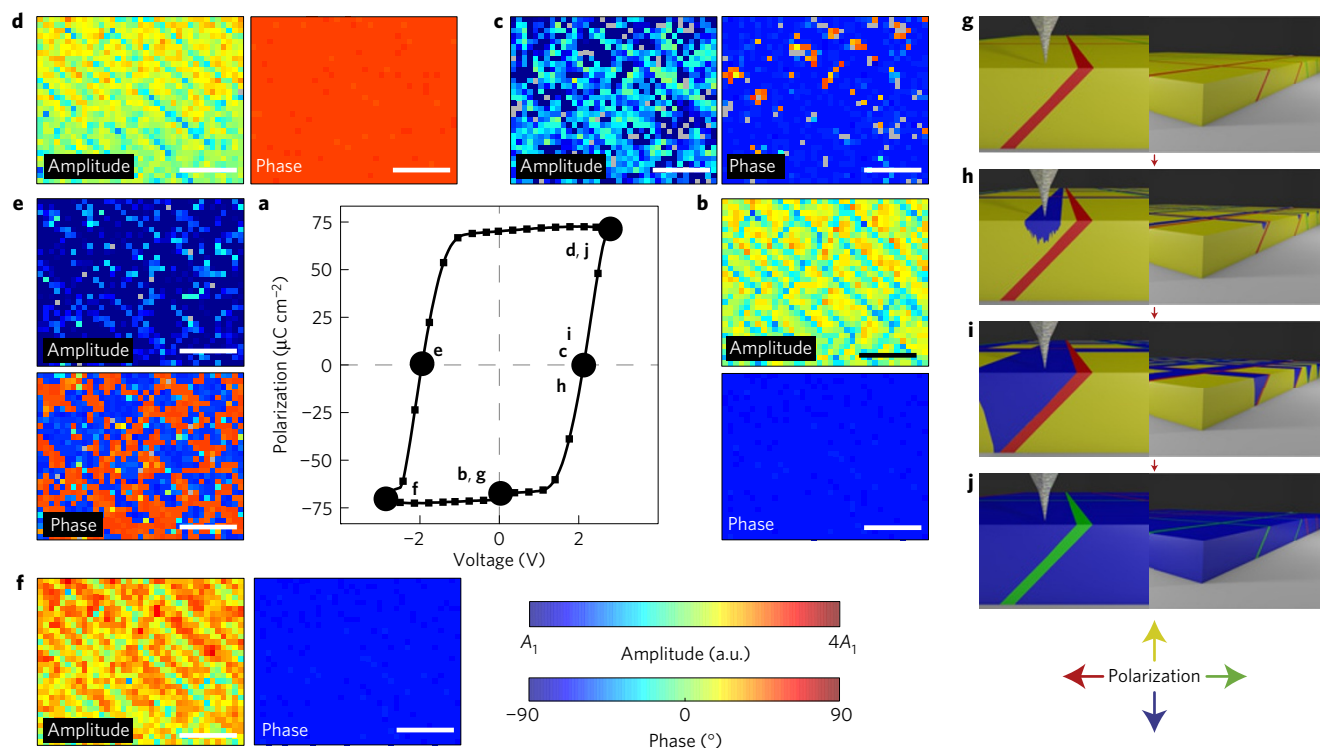


Figure 3 | Understanding switching in $\text{PbZr}_{0.2}\text{Ti}_{0.8}\text{O}_3$ heterostructures. **a**, Typical, macroscopic ferroelectric hysteresis loop of a homogeneous $\text{PbZr}_{0.2}\text{Ti}_{0.8}\text{O}_3$ heterostructure measured at 10 kHz. **b–f**, Corresponding band-excitation switching spectroscopy amplitude and phase images of the same homogeneous $\text{PbZr}_{0.2}\text{Ti}_{0.8}\text{O}_3$ heterostructure measured at various stages (as labelled) of ferroelectric switching. All scale bars are 500 nm. **g–j**, Schematic illustrations of the switching process in the homogeneous $\text{PbZr}_{0.2}\text{Ti}_{0.8}\text{O}_3$ heterostructures. Only the positive-bias half of the switching process is shown. Switching from the down-poled to the up-poled state happens in a similar manner, but with polarization of opposite sense. The colour key on the bottom right labels the polarization directions in the illustrations.

These results are readily explained by conventional theories and observations of ferroelectric switching in homogeneous heterostructures^{26,39}. Starting with the sample in the up-poled state (Fig. 3g), the polarization of the *a* domains is defined by the angle of inclination of the domain wall to avoid forming a charged wall. Ferroelectric switching occurs by nucleating a down-poled *c* domain which tends to nucleate at/near an *a* domain (Fig. 3h). This down-poled domain then grows until being hindered by the presence of a charged 90° domain wall (Fig. 3i). As the bias increases, this *a* domain can undergo 180° switching, eliminating the charged domain wall and allowing the film to switch (Fig. 3j). The final up- and down-poled states are energetically equivalent; therefore, switching in reverse occurs in an identical manner.

In the compositionally graded heterostructures similar BE-SS studies reveal vastly different responses. We show a representative macroscopic ferroelectric hysteresis loop (Fig. 4a; average piezoelectric hysteresis loops are provided, Supplementary Fig. 10) which reveals a significant voltage offset ($\sim 200 \text{ kV cm}^{-1}$). This voltage offset or built-in potential is not the result of an electrode-induced imprint⁴³, but results from the presence of the strain and chemical gradients and other intrinsic sources of symmetry breaking^{41,44–47}.

Local switching studies, starting with the sample in the up-poled state (the self-poling direction, Fig. 4b), reveal enhanced amplitude response within the up-poled *c* domains (compared to the *a* domains), as observed in the homogeneous heterostructures. As a positive bias is applied (Fig. 4c), there is evidence of a change in phase near the domain boundary (orange regions), along with a suppressed piezoresponse in both the *c* and *a* domains, indicative of switching occurring at/near the domain boundaries. Further increasing the positive bias (Fig. 4d) increases the areal fraction of

the switched region (regions of orange phase). We note that there is an enhancement in the local piezoresponse at the *a* domains (compared to the *c* domains). As the bias is reduced (Fig. 4e), the film switches back (driven by the self-poling), causing the *a* domains to reduce their presence, and the piezoresponse appears nearly uniform. Eventually, under a large negative bias, there is no evidence of the domains in the phase image (Fig. 4f). This negative-bias state has an inverse relative local piezoelectric response with respect to the high-field, positive-bias state. The switching process observed is highly asymmetric, with the application of positive and negative fields producing vastly different responses both in the *c* and *a* domains (Supplementary Movie 2).

Using our understanding of the structure and the insights from the BE-SS it is possible to explain the switching process. Starting from the film in the up-poled state (Fig. 4g), application of a positive bias drives the polarization towards the down-poled state. In doing so, owing to the piezoelectric effect, there is a slight decrease in tetragonality (before switching), which drives an increase in *a* domain volume fraction. Whereas changes in the volume fraction of *a* domains are limited in homogeneous heterostructures with parallelepiped-like domains, in compositionally graded heterostructures, however, the needle-like domains can expand towards the free surface (Fig. 4h). Such *c* \rightarrow *a* transitions are associated with large changes in the out-of-plane lattice parameter which translate into large localized piezoresponses at the *a* domains (under a positive bias). As the needle-like domains grow there is an increase in elastic energy, as the shape of the domain deviates from its as-grown state, as well as a reduction in the electrical energy associated with converting the high-energy domain front to an ostensibly uncharged, parallelepiped-like with {101} domain walls. Once the needle-like domains traverse the

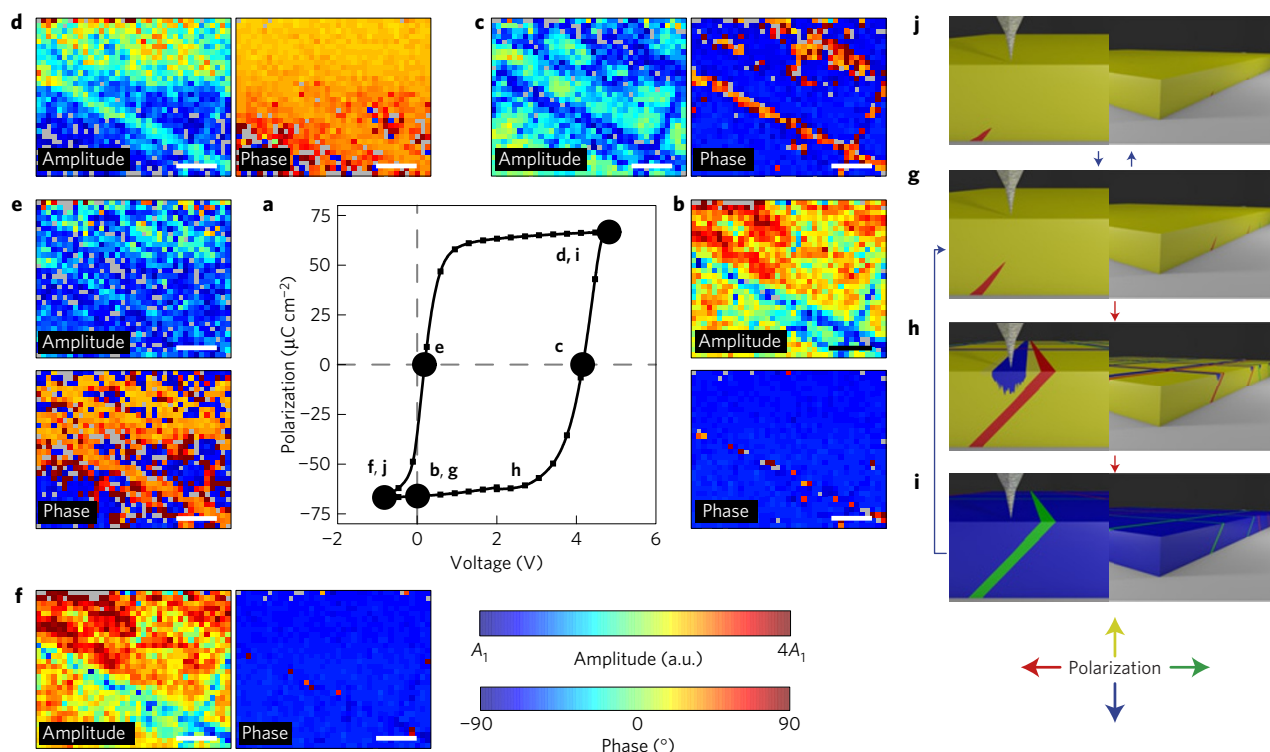


Figure 4 | Understanding switching in compositionally graded heterostructures. **a**, Typical, macroscopic ferroelectric hysteresis loop of a compositionally graded $\text{PbZr}_{1-x}\text{Ti}_x\text{O}_3$ heterostructure measured at 10 kHz. **b–f**, Corresponding band-excitation switching spectroscopy amplitude and phase images of the same compositionally graded $\text{PbZr}_{1-x}\text{Ti}_x\text{O}_3$ heterostructure measured at various stages (as labelled) of ferroelectric switching. All scale bars are 250 nm. **g–j**, Schematic illustrations of the switching process in the compositionally graded $\text{PbZr}_{1-x}\text{Ti}_x\text{O}_3$ heterostructures. The colour key on the bottom right labels the polarization directions in the illustrations.

thickness of the film, it is possible to switch the film to the down-poled state (Fig. 4i, as previously described, Fig. 3i,j). Note that nucleation of a down-poled domain before the *a* domain traversing the film is unlikely because the system would have to overcome the preference for the up-poled state, form a charged domain wall, and transition through a cubic-like state that drives expansion of the needle-like domains. On releasing the bias, a combination of the strong macroscopic self-poling and stored elastic energy drives the film and domain structure to switch back to its initial state (blue arrow, Fig. 4i–g).

Conversely, from the as-grown state, on application of a negative bias, the tetragonality of the film increases owing to the piezoelectric effect, which reduces the necessary volume fraction of *a* domains, causing them to contract (Fig. 4j). Complete removal is unlikely because of the strain state of the film and substrate clamping. We note that *in situ* electrical and structural characterization using TEM of needle-like domains has observed that these domains cannot be completely excluded even under fields approaching the breakdown voltage ($\sim 2,000 \text{ kV cm}^{-1}$; ref. 42). Furthermore, because these ferroelastic domains are typically pinned at the substrate–film interface, as the *a* domains shrink there is an increasing deviation of the domain wall orientation from the ostensibly uncharged $\{101\}$, giving rise to an electrical energy cost which suppresses domain wall contraction. Therefore, given the large associated electrical energy to undergo an $a \rightarrow c$ transition at the ferroelastic domain, we would expect and observe suppressed piezoelectric response within the *a* domains (under a negative bias). On releasing the electric field these domains once again release their stored electrical and elastic energy, returning to their as-grown state.

These differences in the switching process can be highlighted by examining voltage-lapse images of a small section centred around a ferroelastic domain in both the homogeneous (Fig. 5a)

and compositionally graded (Fig. 5b) heterostructures. In the homogeneous heterostructures, we see that switching (phase inversion) occurs abruptly and the amplitude in the *c* domains is universally larger than in the *a* domains. Conversely, in the compositionally graded heterostructures, switching happens more gradually and is localized near the domain boundary. Furthermore, the compositionally graded heterostructures show variations in the relative piezoresponse, having a suppressed piezoresponse in the *a* domains in the as-grown state and under application of a negative bias, but an enhanced piezoresponse under a large positive bias.

Further insight into the switching process can be gained by looking at the shape of the hysteresis loops. In BE-SS, we collect piezoelectric hysteresis loops at each point within a spatial map and fit each of the loops to an empirical model (see Supplementary Fig. 11). Here, we show spatial maps of the magnitude of the negative (E_c^-) and positive (E_c^+) coercive fields and offset (that is, midpoint between these values) for the homogeneous (Fig. 5c) and compositionally graded (Fig. 5d) heterostructures. The homogeneous heterostructures show an increase in the magnitude of the E_c at the *a* domains; however, this increase is symmetric, causing no variance in the offset, indicating that the heterostructure has no preference to be in the up- or down-poled state. In the compositionally graded heterostructures, however, the E_c^- shows near invariance, whereas there is a reduction in E_c^+ near the *a* domains, resulting in a spatially correlated negative offset near the *a* domains, indicating that the *a* domains have a preference to be in their positive bias configuration.

The negligible offset in the homogeneous heterostructures is the result of the fact that the structure is nearly symmetric and the interaction between the *a* and *c* domains is independent of field direction. The response in the compositionally graded heterostructures is more complex. The observed offset at/near the

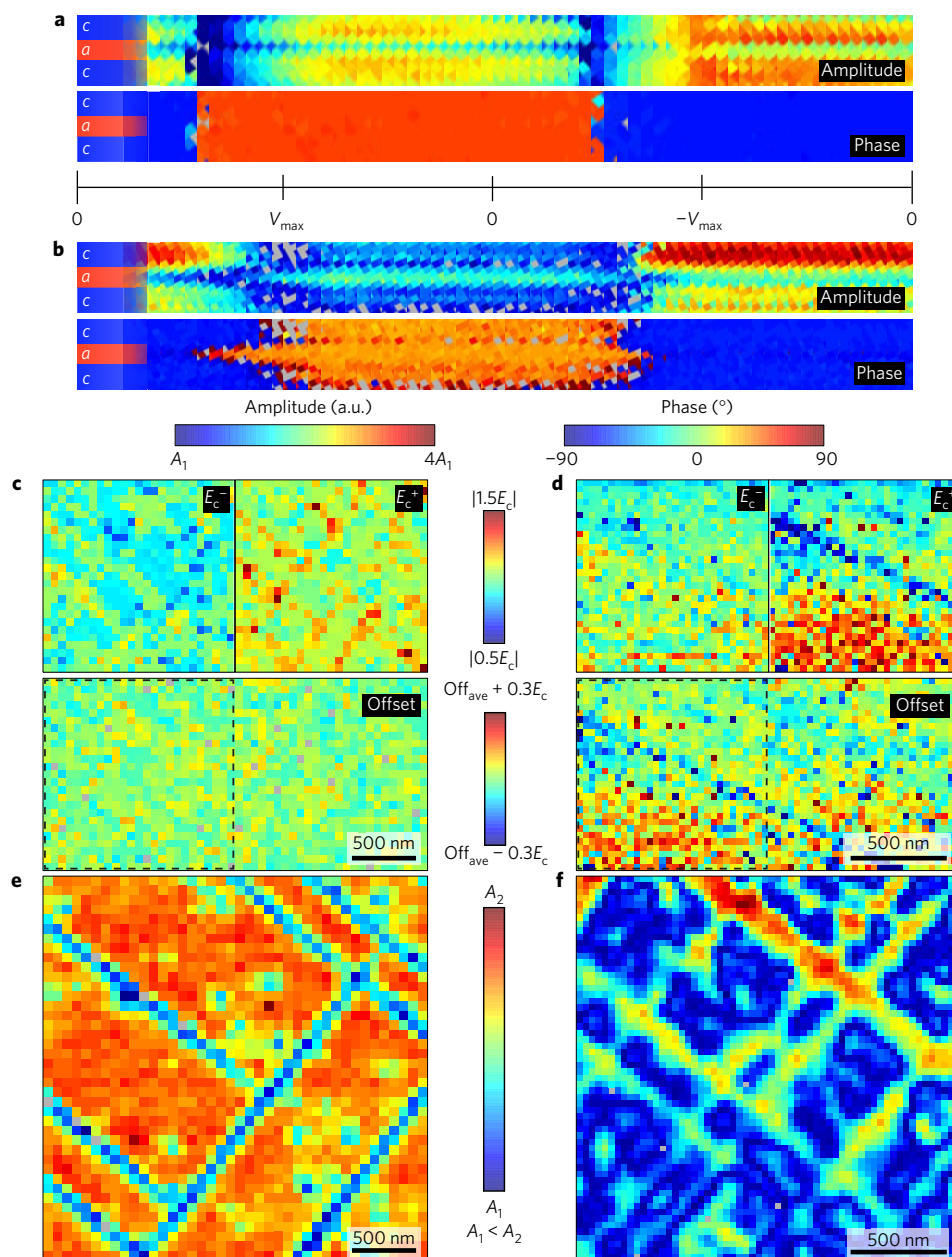


Figure 5 | Breaking down the differences between homogeneous and compositionally graded heterostructures. **a, b**, Voltage-lapse images near an *a* domain in homogeneous $\text{PbZr}_{0.2}\text{Ti}_{0.8}\text{O}_3$ (**a**) and compositionally graded $\text{PbZr}_{1-x}\text{Ti}_x\text{O}_3$ (**b**) heterostructures as imaged throughout a switching cycle. **c, d**, Negative coercive field (E_c^-), positive coercive field (E_c^+) and voltage offset for the same homogeneous $\text{PbZr}_{0.2}\text{Ti}_{0.8}\text{O}_3$ (**c**) and compositionally graded $\text{PbZr}_{1-x}\text{Ti}_x\text{O}_3$ (**d**) heterostructures extracted from fits of piezoelectric hysteresis loops. Colour scales based on an identical fraction of the average fitted coercive field. **e, f**, High-field, local piezoresponse of the same homogeneous $\text{PbZr}_{0.2}\text{Ti}_{0.8}\text{O}_3$ (**e**) and compositionally graded $\text{PbZr}_{1-x}\text{Ti}_x\text{O}_3$ (**f**) heterostructures revealing inverted responses between the two heterostructure variants. All scale bars are 500 nm.

a domains is opposite that of the macroscopic hysteresis loops, a measurement sensitive to the nature of the *c* domains. This suggests that the different domains essentially transfer energy between one another (by changing shape) under an external bias, acting like a ‘spring’ in that each drives the return of the other to the favourable ‘equilibrium’ as-grown state. We propose that the primary energy responsible for this asymmetry is the electrostatic energy. Although there is an elastic energy change under both positive and negative bias, this change is probably similar in magnitude, and thus cannot be used to explain the offset. The electrostatic energy change, however, would be expected to be different because the angle of inclination of the domain wall under negative and positive bias is not the same. Under a

negative bias, the *a* domains are driven to be nearly excluded from the film, causing the domain walls to deviate from the ostensibly uncharged {101} (forming an energetically costly charged domain wall), whereas, under a positive bias, the *a* domains are driven to be parallelepiped-like, which converts a high-energy, charged domain wall to an ostensibly uncharged, low-energy domain wall. This spring-like nature of the ferroelastic domain walls provides a suitable mechanism to explain the anomalous enhancement in built-in potential observed in compositionally graded heterostructures with ferroelastic domains³³. Overall, the spring-like interaction of the *a* and *c* domains demonstrates the importance of the elastic boundary conditions in stabilizing these high-energy and responsive domain structures.

To demonstrate the tangible implications of the observed differences in domain structure and switching mechanics we measured the high-field piezoresponse (at $V_{ac} \approx 1/2E_c$) using BE-PFM for the homogeneous and compositionally graded heterostructures (Fig. 5e,f, respectively). In the homogeneous heterostructures we observe an enhanced piezoresponse within the c domains (as compared to the a domains), as expected. The opposite response is observed in the compositionally graded heterostructures, where the piezoresponse is significantly larger within the a domains (as compared to the c domains). This is a manifestation of the highly labile needle-like ferroelastic domains and the corresponding $c \rightarrow a$ and $a \rightarrow c$ transitions that take place under an applied bias. Such structural transitions produce a locally enhanced piezoresponse, demonstrating the efficacy of compositional and strain gradients in stabilizing highly susceptible, high-energy domain structures.

In summary, compositional and strain gradients were used to modify ferroelastic domain structures, facilitating the design of highly mobile, spring-like domain walls. The compositional and strain gradients preferentially stabilize highly energetic, needle-like domains which, under electrical excitation, are highly labile in the out-of-plane direction (while remaining spatially fixed in the plane) throughout successive field cycling. These labile domain walls give rise to a locally enhanced piezoresponse as a result of the a domains expanding towards the free surface or being nearly excluded from the film (depending on the direction of the applied bias). This work presents new modalities of domain structure engineering through the use of controlled compositional and strain gradients, with significant implications for designing novel forms of ferroelastic domains that are indexable, yet highly mobile. Ultimately, this work demonstrates how compositional and strain gradients can be used to engineer the shape and structure of ferroelastic domains and to control their responses. This has far-reaching implications, as the use of strain-gradient-engineered domain structures can be applied universally to design novel nanoscale functions in (multi-)ferroic materials, facilitating new architectures of domain-wall-based devices.

Methods

Methods and any associated references are available in the [online version of the paper](#).

Received 21 July 2015; accepted 18 January 2016;
published online 15 February 2016

References

1. Roitburd, A. L. Equilibrium structure of epitaxial layers. *Phys. Status Solidi* **37**, 329–339 (1976).
2. Foster, C. M., Pompe, W., Daykin, A. C. & Speck, J. S. Relative coherency strain and phase transformation history in epitaxial ferroelectric thin films. *J. Appl. Phys.* **79**, 1405–1415 (1996).
3. Kwak, B. S. *et al.* Strain relaxation by domain formation in epitaxial ferroelectric thin films. *Phys. Rev. Lett.* **68**, 3733–3736 (1992).
4. Setter, N. *et al.* Ferroelectric thin films: review of materials, properties, and applications. *J. Appl. Phys.* **100**, 051606 (2006).
5. Li, D. & Bonnell, D. A. Controlled patterning of ferroelectric domains: fundamental concepts and applications. *Annu. Rev. Mater. Res.* **38**, 351–368 (2008).
6. Karthik, J., Agar, J. C., Damodaran, A. R. & Martin, L. W. Effect of 90° domain walls and thermal expansion mismatch on the pyroelectric properties of epitaxial $\text{PbZr}_{0.2}\text{Ti}_{0.8}\text{O}_3$ thin films. *Phys. Rev. Lett.* **109**, 257602 (2012).
7. Feigl, L. *et al.* Controlled stripes of ultrafine ferroelectric domains. *Nature Commun.* **5**, 4677 (2014).
8. Chen, L. *et al.* Formation of 90° elastic domains during local 180° switching in epitaxial ferroelectric thin films. *Appl. Phys. Lett.* **84**, 254–256 (2004).
9. Mangalam, R. V. K., Karthik, J., Damodaran, A. R., Agar, J. C. & Martin, L. W. Unexpected crystal and domain structures and properties in compositionally graded $\text{PbZr}_{1-x}\text{Ti}_x\text{O}_3$ thin films. *Adv. Mater.* **25**, 1761–1767 (2013).
10. Seidel, J. *et al.* Conduction at domain walls in oxide multiferroics. *Nature Mater.* **8**, 229–234 (2009).
11. Karthik, J., Damodaran, A. R. & Martin, L. W. Effect of 90° domain walls on the low-field permittivity of $\text{PbZr}_{0.2}\text{Ti}_{0.8}\text{O}_3$ thin films. *Phys. Rev. Lett.* **108**, 167601 (2012).
12. Zednik, R. J., Varatharajan, A., Oliver, M., Valanoor, N. & McIntyre, P. C. Mobile ferroelastic domain walls in nanocrystalline PZT films: the direct piezoelectric effect. *Adv. Funct. Mater.* **21**, 3104–3110 (2011).
13. Karthik, J. & Martin, L. W. Pyroelectric properties of polydomain epitaxial $\text{Pb}(\text{Zr}_{1-x}\text{Ti}_x)\text{O}_3$ thin films. *Phys. Rev. B* **84**, 024102 (2011).
14. Seidel, J. Domain walls as nanoscale functional elements. *J. Phys. Chem. Lett.* **3**, 2905–2909 (2012).
15. Catalan, G., Seidel, J., Ramesh, R. & Scott, J. F. Domain wall nanoelectronics. *Rev. Mod. Phys.* **84**, 119–156 (2012).
16. Farokhipoor, S. *et al.* Artificial chemical and magnetic structure at the domain walls of an epitaxial oxide. *Nature* **515**, 379–383 (2014).
17. Zeches, R. J. *et al.* A strain-driven morphotropic phase boundary in BiFeO_3 . *Science* **326**, 977–980 (2009).
18. Salje, E. & Zhang, H. Domain boundary engineering. *Phase Transit.* **82**, 452–469 (2009).
19. Vasudevan, R. *et al.* Domain wall geometry controls conduction in ferroelectrics. *Nano Lett.* **12**, 5524–5531 (2012).
20. Guyonnet, J., Gaponenko, I., Gariglio, S. & Paruch, P. Conduction at domain walls in insulating $\text{Pb}(\text{Zr}_{0.2}\text{Ti}_{0.8})\text{O}_3$ thin films. *Adv. Mater.* **23**, 5377–5382 (2011).
21. Maksymovych, P. *et al.* Tunable metallic conductance in ferroelectric nanodomains. *Nano Lett.* **12**, 209–213 (2012).
22. Xu, R., Karthik, J., Damodaran, A. R. & Martin, L. W. Stationary domain wall contribution to enhanced ferroelectric susceptibility. *Nature Commun.* **5**, 3120 (2014).
23. McGilly, L. J., Yudin, P., Feigl, L., Tagantsev, A. K. & Setter, N. Controlling domain wall motion in ferroelectric thin films. *Nature Nanotech.* **10**, 145–150 (2015).
24. Su, D. *et al.* Origin of 90° domain wall pinning in $\text{Pb}(\text{Zr}_{0.2}\text{Ti}_{0.8})\text{O}_3$ heteroepitaxial thin films. *Appl. Phys. Lett.* **99**, 102902 (2011).
25. Nagarajan, V. *et al.* Dynamics of ferroelastic domains in ferroelectric thin films. *Nature Mater.* **2**, 43–47 (2003).
26. Roelofs, A. *et al.* Depolarizing-field-mediated 180° switching in ferroelectric thin films with 90° domains. *Appl. Phys. Lett.* **80**, 1424–1426 (2002).
27. Khan, A. I., Marti, X., Serrao, C., Ramesh, R. & Salahuddin, S. Voltage-controlled ferroelastic switching in $\text{Pb}(\text{Zr}_{0.2}\text{Ti}_{0.8})\text{O}_3$ thin films. *Nano Lett.* **15**, 2229–2234 (2015).
28. Feigl, L., McGilly, L., Sandu, C. & Setter, N. Compliant ferroelastic domains in epitaxial $\text{Pb}(\text{Zr,Ti})\text{O}_3$ thin films. *Appl. Phys. Lett.* **104**, 172904 (2014).
29. Wessels, B. W. Ferroelectric epitaxial thin films for integrated optics. *Annu. Rev. Mater. Res.* **37**, 659–679 (2007).
30. Scrymgeour, D. *Ferroelectric Crystals for Photonic Applications* 385–399 (Springer, 2014).
31. Scott, J. F. *Ferroelectric Memories* (Springer Science Business Media, 2000).
32. Scott, J. F. Applications of modern ferroelectrics. *Science* **315**, 954–959 (2007).
33. Agar, J. C. *et al.* Complex evolution of built-in potential in compositionally-graded $\text{PbZr}_{1-x}\text{Ti}_x\text{O}_3$ thin films. *ACS Nano* **9**, 7332–7342 (2015).
34. Mangalam, R. V. K., Agar, J. C., Damodaran, A. R., Karthik, J. & Martin, L. W. Improved pyroelectric figures of merit in compositionally graded $\text{PbZr}_{1-x}\text{Ti}_x\text{O}_3$ thin films. *ACS Appl. Mater. Interfaces* **5**, 13235–13241 (2013).
35. Jesse, S. & Kalinin, S. V. Band excitation in scanning probe microscopy: sines of change. *J. Phys. D* **44**, 464006 (2011).
36. Speck, J. S., Seifert, A., Pompe, W. & Ramesh, R. Domain configurations due to multiple misfit relaxation mechanisms in epitaxial ferroelectric thin films. II. Experimental verification and implications. *J. Appl. Phys.* **76**, 477–483 (1994).
37. Ganpule, C. S. *et al.* Role of 90° domains in lead zirconate titanate thin films. *Appl. Phys. Lett.* **77**, 292–294 (2000).
38. Lee, K., Choi, J., Lee, J. & Baik, S. Domain formation in epitaxial $\text{Pb}(\text{Zr,Ti})\text{O}_3$ thin films. *J. Appl. Phys.* **90**, 4095–4102 (2001).
39. Gao, P. *et al.* Atomic-scale mechanisms of ferroelastic domain-wall-mediated ferroelectric switching. *Nature Commun.* **4**, 2791 (2013).
40. Britson, J., Nelson, C., Pan, X. & Chen, L. First-order morphological transition of ferroelastic domains in ferroelectric thin films. *Acta Mater.* **75**, 188–197 (2014).
41. Catalan, G. *et al.* Flexoelectric rotation of polarization in ferroelectric thin films. *Nature Mater.* **10**, 963–967 (2011).
42. Gao, P. *et al.* Ferroelastic domain switching dynamics under electrical and mechanical excitations. *Nature Commun.* **5**, 3801 (2014).
43. Karthik, J., Damodaran, A. R. & Martin, L. W. Epitaxial ferroelectric heterostructures fabricated by selective area epitaxy of SrRuO_3 using an MgO mask. *Adv. Mater.* **24**, 1610–1615 (2012).
44. Zubko, P., Catalan, G. & Tagantsev, A. K. Flexoelectric effect in solids. *Annu. Rev. Mater. Res.* **43**, 387–421 (2013).

45. Tagantsev, A. K. & Yurkov, A. S. Flexoelectric effect in finite samples. *J. Appl. Phys.* **112**, 044103 (2012).
46. Cross, L. E. Flexoelectric effects: charge separation in insulating solids subjected to elastic strain gradients. *J. Mater. Sci.* **41**, 53–63 (2006).
47. Yudin, P. & Tagantsev, A. Fundamentals of flexoelectricity in solids. *Nanotechnology* **24**, 432001 (2013).

Acknowledgements

J.C.A., G.A.V. and L.W.M. acknowledge support from the National Science Foundation under grant DMR-1451219. A.R.D. and S.P. acknowledge support from the Army Research Office under grant W911NF-14-1-0104. L.R.D. acknowledges support from the Department of Energy, Basic Energy Sciences under grant No. DE-SC0012375 for chemical studies of the materials. R.V.K.M. acknowledges support from the National Science Foundation under grant CMMI-1434147. R.K.V. and S.V.K. acknowledge support from the Division of Materials Sciences and Engineering, Basic Energy Sciences, Department of Energy. Portions of this research were conducted at the Center for Nanophase Materials Sciences, which is a Department of Energy, Office of Science User Facility sponsored at Oak Ridge National Laboratory by the Scientific User Facilities Division, Basic Energy Sciences, Department of Energy which also provided support for M.B.O., S.J. and N.B. J.K. and A.M.M. acknowledge support from the National Science Foundation CMMI/MoM Program under GOALI Grant 1235610. C.G. acknowledges support from the Austrian Science Fund (FWF):[J3397]. Portions of this work were

carried out at the Molecular Foundry, Lawrence Berkeley National Laboratory, which is supported by the US Dept. of Energy under Contract No. DE-AC02-29705CH11231.

Author contributions

J.C.A. and L.W.M. designed the experiments. J.C.A., R.V.K.M. and G.A.V. grew the films and conducted the macroscopic electrical and structural characterization. L.R.D. completed the Rutherford backscattering spectrometry studies. J.K., C.G. and A.M.M. prepared the samples for STEM and conducted the STEM imaging and nanobeam diffraction strain mapping. J.C.A., J.K., C.G., A.M.M. and L.W.M. analysed the STEM and nanobeam diffraction strain mapping data. M.B.O., S.J., N.B. and S.V.K. designed the custom band-excitation system. J.C.A., M.B.O. and R.K.V. conducted the band-excitation measurements. M.B.O., S.J., R.K.V. and S.V.K. designed the band-excitation fitting and piezoelectric loop fitting algorithm and software. J.C.A., M.B.O., R.K.V., S.J., N.B., S.V.K. and L.W.M. analysed the band-excitation results. J.C.A., A.R.D., S.P. and L.W.M. determined the switching mechanism. J.C.A. and L.W.M. co-wrote the paper.

Additional information

Supplementary information is available in the [online version of the paper](#). Reprints and permissions information is available online at www.nature.com/reprints. Correspondence and requests for materials should be addressed to L.W.M.

Competing financial interests

The authors declare no competing financial interests.

Methods

Heterostructure design and film growth. Homogeneous and compositionally graded $\text{PbZr}_{1-x}\text{Ti}_x\text{O}_3$ heterostructures were grown using pulsed-laser deposition from $\text{Pb}_{1.1}\text{Zr}_{0.2}\text{Ti}_{0.8}\text{O}_3$ and $\text{Pb}_{1.1}\text{Zr}_{0.8}\text{Ti}_{0.2}\text{O}_3$ targets. The compositional gradients result in an increasing bulk in-plane lattice parameter as one transitions from the bottom to the top of the film. All heterostructures studied herein are grown on 30-nm $\text{SrRuO}_3/\text{GdScO}_3$ (110) substrates (lattice parameters $a = 5.45 \text{ \AA}$, $b = 5.75 \text{ \AA}$ and $c = 7.93 \text{ \AA}$; pseudocubic $a_{\text{pc}} = 3.973 \text{ \AA}$), which produces an effective lattice mismatch that varies from 0.8% to -3.5% from the substrate to film surface in the compositionally graded heterostructures (Supplementary Fig. 1). All films were grown using pulsed-laser deposition following established procedures. Briefly, the bottom electrode SrRuO_3 films were grown at 630°C in an oxygen pressure of 100 mtorr at a laser fluence of 1.8 J cm^{-2} and a frequency of 13 Hz. The compositionally graded $\text{PbZr}_{1-x}\text{Ti}_x\text{O}_3$ layers were grown at 600°C in an oxygen pressure of 200 mtorr at a laser fluence of 1.9 J cm^{-2} and a frequency of 3 Hz. The composition of the compositionally graded layers was controlled by continuously varying the composition from $\text{PbZr}_x\text{Ti}_{1-x}\text{O}_3$ to $\text{PbZr}_y\text{Ti}_{1-y}\text{O}_3$ using a programmable target rotator (Neocera, LLC) that was synced with the excimer laser. For all the samples, films were cooled in an oxygen pressure of 700 torr following growth.

For macroscopic measurements, symmetric capacitor structures were fabricated by subsequent deposition of 80-nm SrRuO_3 top electrodes defined using a MgO hard-mask process⁴³. Rutherford backscattering spectrometry reveals the presence of smooth compositional gradients in the films (Supplementary Fig. 2). $\theta-2\theta$ X-ray diffraction studies reveal that all films are fully epitaxial, 00 l -oriented, and single-phase (Supplementary Fig. 3). Asymmetric reciprocal space mapping (RSM) studies reveal that both the homogeneous and compositionally graded heterostructures are nearly coherently strained to the substrate, resulting in a strain gradient in the compositionally graded heterostructures which approaches $4.3 \times 10^5 \text{ m}^{-1}$ (Supplementary Fig. 4).

Scanning probe measurements. All atomic force microscopy studies were performed at the Center for Nanophase Materials Science at Oak Ridge National Laboratory using a custom Cypher microscope (Asylum Research) controlled with a Labview- and Matlab-based band-excitation controller. The use of band excitation for these measurements is crucial as it minimizes effects from changing tip-sample contact resonances that can alter the observed response, enabling the measurement of piezoresponse to be consistent throughout multiple dimensions

(that is, frequency, spatial, voltage, time, and so on; see Supplementary Fig. 5). All measurements were carried out using Pt/Cr-coated probe tip (Budget Sensors, Multi75E-G). BE-PFM imaging studies were conducted at a centre frequency of $\sim 330 \text{ kHz}$ (with a BE bandwidth of 60 kHz) and $\sim 680 \text{ kHz}$ (with a BE bandwidth of 60 kHz) for the vertical and lateral images, respectively. The sensing BE waveform for all imaging studies was of chirp character with a V_{pp} (peak-to-peak) of 1 V. Switching spectroscopy measurements were measured at a resonance frequency of $\sim 330 \text{ kHz}$ (with a BE bandwidth of 60 kHz). The d.c. voltage was chosen such that the piezoelectric hysteresis loops were saturated in both the positive and negative direction. The local piezoresponse was measured at remanence (following a dwell time of 0.5 ms) with a BE waveform of sinc character with a V_{pp} of 0.75 V. Unlike conventional PFM techniques which measure the local piezoresponse with a scanning probe at a single or dual frequencies near the cantilever resonance, BE-PFM measures piezoresponse using a frequency band near the cantilever resonance, enabling direct measurement of the full cantilever resonance characteristics.

HAADF-STEM imaging and nanobeam diffraction. All measurements were completed at the National Center of Electron Microscopy at Lawrence Berkeley National Laboratory. Cross-sectional samples were prepared using the focused-ion beam machining lift-out technique and subsequently attached to a Cu grid. Final polishing was done in a nanomill using a 500 eV argon beam. Samples were first inspected by bright-field imaging in a JEOL 3010 operated at an accelerating voltage of 300 kV. Elastic strain and local crystal rotation mapping about the domain structures was conducted using nanobeam diffraction in an FEI Titan, also operated at 300 kV. Individual diffraction patterns were collected at 2.5 nm intervals over a $160 \text{ nm} \times 160 \text{ nm}$ region. Diffraction peak locations were identified relative to a reference pattern using cross-correlation analysis, which were then used to calculate the local elastic strain and crystal rotation. Further details of the elastic strain mapping approach can be found in ref. 48. This analysis approach allows the full resolution of the two-dimensional strain tensor over large areas, relative to other standard techniques such as geometric phase analysis.

References

- Ozdol, V. B. *et al.* Strain mapping at nanometer resolution using advanced nano-beam electron diffraction. *Appl. Phys. Lett.* **106**, 253107 (2015).